Robotectonics: Emergent Phototactic Aggregation-Disaggregation in Swarms

Fabio Giardina,[1,*] S. Ganga Prasath,[1,2,*] and L. Mahadevan[1,3,4,†]

[1]*School of Engineering and Applied Sciences, Harvard University, Cambridge, Massachusetts 02138, USA*
[2]*Department of Applied Mechanics & Biomedical Engineering, IIT Madras, Chennai 600036, Tamil Nadu, India*
[3]*Department of Physics, Harvard University, Cambridge, Massachusetts 02138, USA*
[4]*Department of Organismic and Evolutionary Biology, Harvard University, Cambridge, Massachusetts 02138, USA*

(Received 30 June 2025; accepted 4 February 2026; published 10 April 2026)

The collective construction of complex architectures by social insects involves the use of decentralized spatiotemporal signals in a dynamical environment that changes the behavior of the insects and is changed by them. Inspired by this original example of "stigmergy," we show that a robot collective can nucleate, construct, and deconstruct aggregates via a trapping instability by simply altering their local transport behavior. We quantify these observations in terms of a two-dimensional phase space that encompasses agent-agent interaction and the agent-environment interaction (collection and deposition). Our results show how coordinated function can emerge spontaneously through simple local rules for sensing and action without the need for global representation, planning, or optimization/control algorithms, in sharp contrast with the traditional views of complex task execution. More broadly, our study shows that embodied collectives can leverage the environment as both a communication channel and a spatiotemporal memory, coupling organismal behavior to environmental remodeling leading to "exbodied intelligence."

DOI: 10.1103/cx3h-bwhc

I. INTRODUCTION

How do large decentralized collections solve problems far beyond the scale of their individual members—constructing multiscale architectures, hunting large prey, or defending against predators? Both natural systems such as insect colonies [1–5] and artificial ones such as robotic swarms [6–12] rely on the wisdom of the collective to accomplish tasks no single member can. Social insects—ants, bees, termites, and wasps—build elaborate structures without centralized control, adapting to variable environments through local interactions and feedback. Each individual performs simple actions in response to environmental cues, which in turn modify group behavior. This continuous feedback between the agents and their surroundings creates functional spatial patterns representing a collective "exbodied" intelligence.

One prominent example of this decentralized coordination is *stigmergy*, first observed in social insects [3,4,13,14]. Stigmergy occurs when agents leave signals (e.g., pheromones) that guide the actions of others, forming a dynamic communication network. This triadic interaction between agents, signals, and environment—each evolving dynamically as the task progresses [1,2] [see Fig. 1(a)]—produces coordination without central control. Inspired by these natural systems, engineers have tried to replicate similar behavior in robotic swarms [3,4,15–19]. While these artificial systems show promise in generating cooperative behaviors, they often lack the robustness and adaptability seen in nature. This gap is partly due to the fact that most robotic approaches focus on the agent behavior, and treat the environment as static rather than as a dynamic field that shapes and is shaped by collective behavior.

To bridge this gap between the natural and the artificial [20–29], we integrate robotic agents with a dynamically changing environment [5,7,11,30,31] to study how collectives build and dismantle large-scale structures—a process we call *robotectonics*. Through theoretical modeling and real-world robotic experiments, we show how simple local rules yield adaptable task execution via collective behavior.

II. ROBOTIC ANTS

To simulate the aggregation tasks performed by social insects, which use pheromones to guide their building and remodeling activities, we developed a swarm of robotic ants (RAnts), building upon our previous research inspired by the excavation behaviors (or disaggregation) of ants [5]. In this article, we define the aggregation process as the transportation of substrate elements from one part of the domain to another. The resulting aggregates may have functional properties, such as those seen in termite mounds, when the effects of selection pressure induced by the environment, e.g., via diurnal or seasonal changes in the temperature that lead to certain morphologies being preferred over others, are taken into account. Here we do not distinguish between different functional structures, as selecting between them would involve the

*These authors contributed equally to this work.
†Contact author: lmahadev@g.harvard.edu

Published by the American Physical Society under the terms of the Creative Commons Attribution 4.0 International license. Further distribution of this work must maintain attribution to the author(s) and the published article's title, journal citation, and DOI.

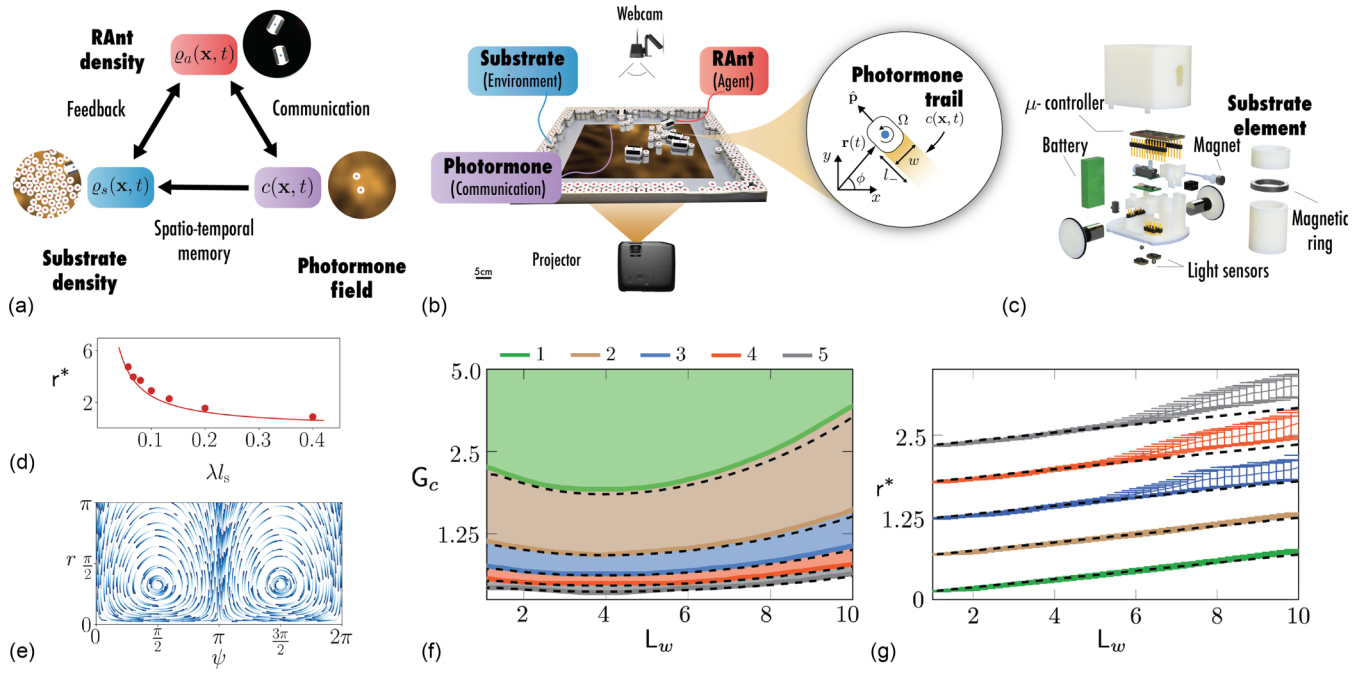


FIG. 1. Single-agent behavior and trapping instability. (a) Triadic interactions in the model and experiments: RAnt density $\varrho_a(\mathbf{x},t)$ represents the agent field, photormone field $c(\mathbf{x},t)$ is the communication field, and the substrate density $\varrho_s(\mathbf{x},t)$ [see Eqs. (8)–(10)] serves as the environment. Agents interact with each other and the substrate haptically and phototactically. Regions of high photormone concentration serve as nuclei where aggregation begins and gets reinforced by repeated RAnt visits. (b) Robotic platform for aggregation and disaggregation experiments involves an arena where the RAnts move and communicate with each other via *photormone field* that they generate along their trajectory. A webcam tracks the position of individual RAnts and is used to compute the photormone production via Eq. (5), which is then displayed on the working surface of the robots using a projector. Each RAnt is described by its position $\mathbf{r}(t)$, orientation $\hat{\mathbf{p}}$ [see Eqs. (3) and (4)], and it leaves behind a trail of photormone $c(\mathbf{x},t)$ of width w [described in Eq. (5)]. It also responds to gradients in the photormone field that it encounters, by rotating at a speed Ω, proportional to the gradient along the normal direction. l_- is the lengthscale over which the photormone decays, and l_s is the distance between the light sensors [also in Eq. (5)]. (c) RAnts are autonomous wheeled robots and are equipped with two light sensors to measure the local photormone intensity (gradient information) and a servomotor equipped with a magnet to transport substrate elements. The substrate element has a magnetic ring that enables easy attachment and detachment from the RAnts. (d) Characteristic scaled radius of the circle, $\mathsf{r}^* = r^*/l_s$, along which the RAnt moves as measured in experiments by projecting a field of constant gradient of strength λ as discussed in Eqs. (3) and (4). (e) Phase-space (ψ, r) of the single RAnt dynamics with fixed points (ψ^*, r^*) [also from Eqs. (3) and (4)]. (f) Phase-diagram capturing the trapping instability for multiple RAnts represented using the nondimensional critical gain, G_c, of each RAnt vs the scaled photormone production width, $\mathsf{L}_w = w/l_s$, described by Eq. (6) (g) Radius of trapping, $\mathsf{r}^* = r^*/l_s$, for different numbers of RAnts (1–5) as a function of the scaled photormone production width, L_w. Dashed lines show the theoretical predictions corresponding to $\mathsf{r}^* = (\mathsf{L}_w + 1)/4$ and the simulations are the colored lines. Note that the trapping radius for different numbers of RAnts is vertically offset for visualization purposes.

relative functional merits of different types of aggregates. Instead, we focus only on the self-organized emergence of collective aggregation and disaggregation.

Our robots are equipped with phototactic sensors to detect light-based signals, mimicking how ants sense pheromone gradients. To enable them to physically interact with their environment, the RAnts can lift and transport cylindrical objects [see Figs. 1(b) and 1(c)]. Each RAnt is designed to (see Appendix 1 for further details) (i) generate and leave behind a dynamic communication signal/field that can be sensed by other agents; (ii) identify and move the construction materials; and (iii) modify its behavior in response to sensing the communication signal.

The robotic platform Fig. 1(b) is designed to simulate collective behaviors in an enclosed arena where our wheeled RAnts can move freely while creating and responding to a simulated pheromone field, called a *photormone* field. This field, derived from the Greek cognates *photo*, meaning light, and *hormon*, meaning stimulating, is generated through light projection onto a translucent screen, and the screen is the ground on which the agents move. Similar field-driven collective robot dynamics has been explored in other studies [7,29], but unlike previous studies that have employed similar light-sensing setups [26,32], our approach uses this field as a spatiotemporal field to store and retrieve dynamical information in the environment to execute a collective task.

Each battery-powered RAnt has an onboard microcontroller encoded with behavioral rules to sense, move, and build/unbuild (see Fig. 2) (see Appendix 1 for more details). Two light sensors can detect the intensity of the photormone field and infer direction of travel [see Fig. 1(b) and Appendix 2 for more details), and the RAnt can move and turn using two independently controlled wheels, while being able to also detect obstacles in front of them with an infrared sensor. The light sensors below the RAnts are placed along their width, close to their wheels, so that they can measure the instanta-

Algorithm 1 RAnt local rules

```
d ← 1
K ∈ [−1, 1]
C ∈ [0, 1]
c̄ ← 0.4 c_max
Δc ← 0.2 c_max
while true do
    c, ∇c ← get local photormone value and gradient
    heading ← f(∇c, C, d)
    if object detected then
        if d = 1 then
            X ← true with probability |K|
            if X and KCc < K(c̄ − KΔc) then
                fetch object
                d = −1
            else
                turn away from object
            end if
        else if d = −1 and Kc > CK(c̄ + KΔc) then
            disengage magnet
            turn away from object
            d = 1
        else
            continue
        end if
    else
        d = 1
        disengage magnet
    end if
end while
```

FIG. 2. Pseudocode of internal robot rules. We start by initializing all relevant parameters, namely the movement direction d (1 for forward with engaged magnet, –1 for backward with disengaged magnet), the deposition rate K, the cooperation parameter C, and the threshold parameters $\bar{c}$ and Δc that together determine when the robots pick up or deposit an object (substrate). The behavioral loop can be broken down into four parts. First, a robot measures the local photormone concentration c and its gradient ∇c and updates its heading as a function of ∇c, C, and d (see Appendix 2 for the implementation of f). Second, as the robot moves and detects an obstacle, it decides to either (i) pick it up with probability proportional to $|\mathsf{K}|$ if the threshold condition is reached, or (ii) avoid it otherwise. Third, the robot releases captured objects when the (hysteretic) threshold condition is reached. Fourth, and finally, in the absence of any obstacles, the robot disengages the magnet.

neous gradients across the wheels and thus control the steering directly. Additionally, they have a retractable magnet to attach and detach from cylindrical PVC building blocks fitted with a magnetic ring inclusion [see Fig. 1(c)]. This combination of internal behavioral rules (example shown in Fig. 2) and the exbodied collective interactions between the RAnts and the environment leads to the emergence of coordinated group behaviors, allowing the RAnts to build and dismantle structures by communicating using dynamic photormone patterns.

III. INDIVIDUAL RANT BEHAVIOR

A. Single RAnt in static photormone field

The extent to which robots respond to an external photormone field can be controlled by a nondimensional number we call the cooperation parameter, $\mathsf{C} \in [0, 1]$; a random walk corresponds to $\mathsf{C} = 0$, while perfect gradient-following corresponds to $\mathsf{C} = 1$ (implementation details are described in Appendix 2). When $\mathsf{C} = 1$, each RAnt's position $\mathbf{r}(t)$ and orientation $\hat{\mathbf{p}}(t)$ [see Fig. 1(b), inset] evolves according to the following equations:

$$\dot{\mathbf{r}}(t) = v_o \hat{\mathbf{p}}(t), \tag{1}$$

$$\dot{\hat{\mathbf{p}}}(t) = \Omega \times \hat{\mathbf{p}}(t). \tag{2}$$

Here the orientation is given by $\hat{\mathbf{p}}(t) = (\cos\theta(t), \sin\theta(t))$, $\theta(t)$ is the heading angle, and v_o is the base speed of the RAnt. RAnts can sense the gradient in a photormone field $c(\mathbf{x}, t)$, which causes the RAnts to reorient at a rate $\Omega = G(\nabla c \cdot \hat{\mathbf{n}})\hat{\mathbf{z}}$, where $\hat{\mathbf{n}} = (-\sin\theta, \cos\theta)$, $\hat{\mathbf{z}}$ is the out-of-plane direction, and G is the rotational gain. The rotation rate Ω being a function of the gradient along the agent's width is inspired by ants being able to measure gradients with their antennae on either side of their head. In a constant gradient with $\nabla c = -\lambda \hat{\mathbf{r}}$, writing $\hat{\mathbf{r}} = (\cos\phi, \sin\phi)$ with ϕ being the polar angle relative to a laboratory axis, the rotation rate becomes $\Omega = G\lambda \sin(\theta - \phi)\hat{\mathbf{z}}$. The dynamical equations of motion can be written in nondimensional form by scaling lengths using the intrinsic lengthscale from the prescribed gradient λ^{-1} and time using the intrinsic timescale $1/(v_o\lambda)$. In the transformed variables $r \to r/\lambda, t \to t/(v_o\lambda)$, the evolution Eqs. (1) and (2) become (after dropping tildes)

$$\dot{r} = \cos\psi, \tag{3}$$

$$\dot{\psi} = \left(\mathsf{G} - \frac{1}{r}\right)\sin\psi, \tag{4}$$

where $\psi = (\theta - \phi)$, $\mathsf{G} = G/v_o$ is the photormone sensitivity, and $r(t) = ||\mathbf{r}(t)||$ is the radial distance of a given RAnt. We see that Eqs. (3) and (4) have a fixed point in the dynamics at $r^* = 1/\mathsf{G}$, $\psi^* = \pi/2$ and correspond to a circular trajectory with constant radius $r = r^*$, as seen in Fig. 1(e) in the (ψ, r)-plane.

To test this simple prediction, we use our robotic platform [shown in Fig. 1(b)] to address how RAnts move in a stationary photormone field with a constant gradient, $c = -\lambda r$; indeed, a RAnt moves in a circle of radius $1/\mathsf{G}$ (see SM Video 1). In Fig. 1(d) we show that the experimentally measured r^* versus λ, scaled using the distance between light sensors l_s, is consistent with the scaling result $r^* \sim \mathsf{G}^{-1}$. Perturbations of the RAnt dynamics with initial conditions away from this fixed point result in quasiperiodic dynamics with precession of the RAnt orientation as shown in the phase-space of the RAnts defined in the (ψ, r)-plane [see Fig. 1(e) and SM Sec. II A [33] for further details about the dynamics of single RAnt].

B. RAnts in a dynamic photormone field

To allow the photormone field to evolve in response to the motion of RAnts, we now assume that the agents can actively produce photormone at a rate k_+, and that the field decays over time at a constant rate k_-. The photormone field $c(\mathbf{x}, t)$ then evolves according to

$$\partial_t c(\mathbf{x}, t) = k_+ \varrho_a[\mathbf{r}, w] - k_- c(\mathbf{x}, t), \tag{5}$$

where $\varrho_a = \{1 \text{ if } |\mathbf{x}-\mathbf{r}|^2 \leqslant w^2;\ 0 \text{ if } |\mathbf{x}-\mathbf{r}|^2 > w^2\}$ is the RAnt density that has a unit magnitude in a circle surrounding the agent with a width w where the photormone is produced, and zero elsewhere. Equations (1), (2), and (5) complete the formulation of a RAnt that deposits a decaying photormone field and in turn responds to it.

The dimensional Eq. (5) has the three lengthscales: l_s, w, and $l_-(= v_o/k_-)$, where l_s is the physical distance between the light sensors on the RAnts, w is the radius over which photormone is produced, and l_- is the lengthscale over which the RAnts travel before the photormone they generate decays e-fold [see Fig. 1(b) inset for a schematic]. We can define two nondimensional numbers using these lengthscales as $\mathsf{L}_- = l_-/l_s$, $\mathsf{L}_w = w/l_s$. In the two limits of scale-separation given by $\mathsf{L}_- \ll \mathsf{L}_w \sim 1$ and $\mathsf{L}_w \sim 1 \ll \mathsf{L}_-$, we shall see that for cooperation parameter $\mathsf{C} = 1$ (defined later), the RAnt is trapped in its photormone field, whereby its trajectories are bound orbits (which we call *traps*). These behaviors have long been known in biology in such contexts as the milling behavior observed in some types of ants [34], who follow a reinforced pheromone trail until they die of exhaustion.

When the lengthscale over which pheromone decays l_- is small relative to the width of photormone generation w, this corresponds to $\mathsf{L}_- \ll \mathsf{L}_w$. The gradient measured by the sensor is then determined by the size over which they generate photormone, i.e., w. In this limit, the maximum gradient measured by a RAnt as it generates photormone is at the specific location $\mathsf{r}^* = (\mathsf{L}_w + 1)/4$, where $\mathsf{r} = r/l_s$ (see SM Sec. II B for details) and is expected to be the radius of the bound orbit. We see that the radius of self-trapping is purely geometric when we are in the limit of $\mathsf{L}_- \ll \mathsf{L}_w$ as the trapping radius depends only on the size of photormone production w and the distance between sensors. However, for this distance to be the radius of trapping realizable in experiment, we need to ensure that the RAnts are capable of making such a turning radius. From our earlier analysis for constant gradient in Eqs. (3) and (4), we know that the critical radius is $\mathsf{r}_c = 1/(\mathsf{G}\nabla c)$. Therefore, in order for the trapping radius r^* to be realizable, we require that it be greater than or equal to the critical turning radius r_c, i.e., $\mathsf{r}^* \geqslant \mathsf{r}_c$. We can identify the boundary of self-trapping using the conditions $\mathsf{r}^* = \mathsf{r}_c$. This provides us with the critical gain G_c required for the RAnts to self-trap at a radius r^* for a given L_w.

We arrive at the expression for G_c by first finding the steady-state photormone intensity assuming a RAnt travels along a circle of radius r^* by solving Eq. (5). Using the steady-state profile, we calculate the gradient around this trajectory subject to the compatibility turning condition, $\mathsf{r}^* \geqslant \mathsf{r}_c$. We briefly outline the calculation here, and the details are in SM Sec. II B. For a given r^*, the steady-state photormone concentration of Eq. (5) closer to the center of the trap is expected to be a constant $c = k_+/k_- = k_\pm$. This is because the limit $\mathsf{L}_w \gtrsim 1$ implies that the photormone production diameter w is large enough to cover the circle drawn by the trajectory of the sensor. Hence, for the sensor closer to the center, the measured photormone value is governed by Eq. (5) with $\varrho_a = 1$: $\dot{c} = k_\pm - c$, where we have nondimensionalized Eq. (5) by using $(1/k_-)$ as the timescale and l_s as the lengthscale. The outer sensor, on the other hand, travels along a circle of radius $\mathsf{R} = (\mathsf{r}^* + 1)/2$ [see SM Fig. S1(d) for a schematic] and "sees" photormone production only for a fraction of the inner sensor. After solving for the photormone field in Eq. (5), we get $\nabla c = [c(\mathsf{R}) - k_\pm]$. The value of photormone at the outer sensor converges to

$$c(\mathsf{R}) = k_\pm\left[1 - \exp\left(\frac{\tau_1}{2}\right)\frac{\exp(\tau_2)-1}{\exp(\tau_1+\tau_2)-1}\right],$$

where τ_1 is the time over which RAnts produce photormone as they traverse the circle, and $\tau_1 + \tau_2 = 2\pi\mathsf{r}^*/\mathsf{L}_-$ is the time taken to go around the circle r^* once. Ultimately, we arrive at the expression for critical gain of each RAnt to trap given by

$$\mathsf{G}_c = \frac{1}{k_\pm - c(\mathsf{R})} = \left[\exp\left(\frac{\tau_1}{2}\right)\frac{\exp(\tau_2)-1}{\exp(\tau_1+\tau_2)-1}\right]^{-1}. \quad (6)$$

In the limit when $\mathsf{L}_w \gg 1$, we can arrive at the asymptotic behavior of the critical gain, G_c (as (described in detail in SM Sec. II B), and we get

$$\mathsf{G}_c \approx \frac{4\mathsf{L}_-}{\mathsf{L}_w k_\pm}\sinh\left(\frac{\pi\mathsf{L}_w}{4\mathsf{L}_-}\right). \quad (7)$$

On the other hand, when $\mathsf{L}_w \ll \mathsf{L}_-$, the geometry associated with the generation of photormone no longer affects the trapping dynamics. In this limit, we expect the radius of trapping to be large, and from a similar analysis we find that $\mathsf{r}^* \approx \mathsf{L}_w\mathsf{G}k_\pm/2\pi$ [see SM Fig. S1(e) for comparison between the prediction and full solution in Eq. (6)]. The trapping conditions for a given field dynamics, i.e., fixed $k_\pm$, thus depends on the photormone sensitivity and agent's mobility through G, the geometry of the sensor arrangement, and photormone production through L_w, L_-.

To summarize, when $\mathsf{L}_- \ll \mathsf{L}_w$, the trapping radius is $\mathsf{r}^* = (\mathsf{L}_w + 1)/4$ as long as $\mathsf{r}^* > \mathsf{r}_c$. We can ensure this by choosing $\mathsf{G}_c = 1/[k_\pm - c(\mathsf{R})]$. On the other hand, when $\mathsf{L}_w \ll \mathsf{L}_-$, the trapping radius is $\mathsf{r}^* \approx \mathsf{L}_w\mathsf{G}k_\pm/2\pi$. We have described here the trapping conditions required for a single RAnt while the condition for multiple RAnts in a collective field is discussed in the SM Sec. II B [see also Fig. 1(f)]. Trapping results from a buildup of photormone in a confined region of space and stops a RAnt from exploration. We can avoid trapping of a single agent by setting the internal gain G_c below the theoretical predictions and thus have control over the number of agents that must be within the trapping radius to start a trap (see SM Video 2 for single agent trapping and SM Video 3 for multiagent trapping in experiments). Our results are qualitatively similar to earlier studies on trapping in a single agent [35–37] as well multiple agents [38] that show similar trapping mechanisms. As we shall see later, the trapping instability we have analyzed here acts as a mechanism for spontaneous seed formation for aggregation: a trap made by a number of agents forms an effective attractor that can be exploited to spatially coordinate the aggregation effort.

IV. COLLECTIVE BEHAVIOR OF RANTS

A. Algorithm for collective robotectonics

Two important mechanisms intrinsic to RAnts facilitate collective aggregation: (i) ability to follow gradients or phototaxis, (ii) a thresholded response to photormone which sets the criteria for consensus of the agents. While the phototaxis

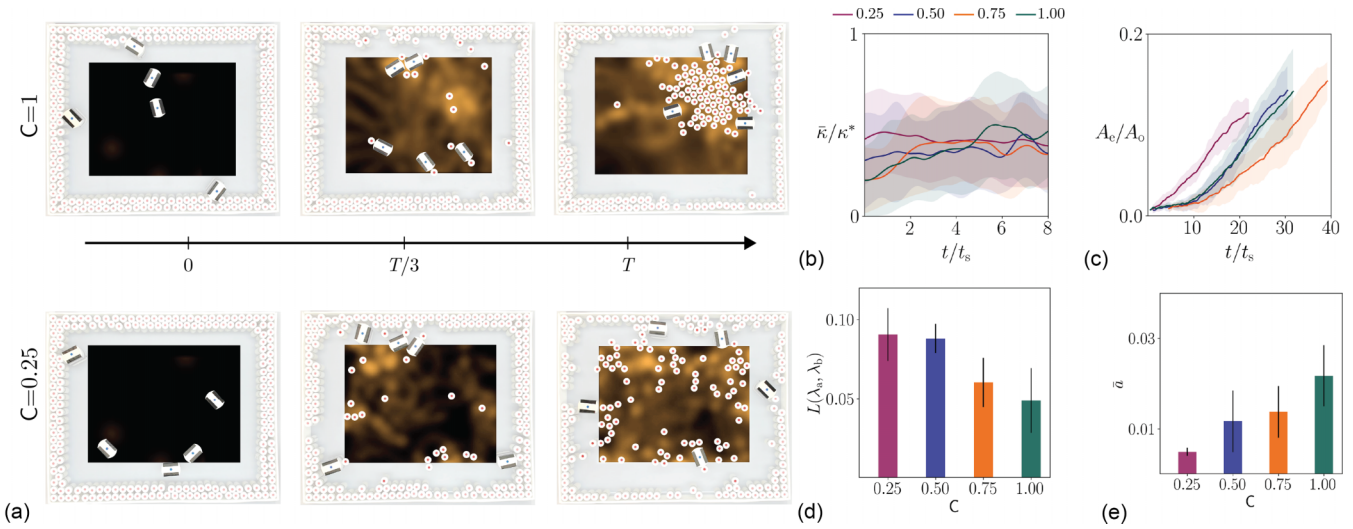


FIG. 3. Collective robotic aggregation. (a) Snapshots of robot aggregation progression in experiments at different times for cooperation parameters $\mathsf{C} = 0.25$ and 1, showing that an increase in C drives collective aggregation. (b) Nondimensional average curvature of the RAnts' trajectories, $\bar{\kappa}/\kappa^*$, with κ^* being the inverse of the trapping radius, as a function of normalized time and for different cooperation parameters C (whose values are shown above the figure). t_s is the time it takes for a RAnt to cross the arena. (c) Normalized covered area of deposited substrate A_e/A_o (A_o aggregation area) as a function of time and for different cooperation parameters C [same color coding as in (b)]. (d) Circumference L of the ellipse defined by the eigenvalues λ_a, λ_b of the sample covariance matrix of the substrate elements in the aggregation area as a function of the cooperation parameter C. (e) Average cluster area relative to aggregation area $\bar{a} = (n_c A_o)^{-1} \sum_{i=1}^{n_c} A_i$ as a function of the cooperation parameter C. n_c is the number of clusters, A_0 the area of the aggregation arena, and A_i the area covered by the ith cluster (see SM Sec. VI for the final position of the substrate and n_c as a function of C).

ability is important for a directed motion towards the aggregation seed, the threshold criteria for consensus helps to coordinate the collective effort by using the photormone concentration as a spatiotemporal memory of the previous activity of the collective. How can we encode these behaviors into a set of rules for the RAnts to follow?

In Fig. 2, we provide a behavioral algorithm for collective aggregation. A short summary of the algorithm follows: (i) the main loop, *set heading*, determines the rotation of the robot, which is a function of the local photormone gradient, ∇c, the cooperation parameter C, and the direction of travel d; (ii) simultaneously the robot uses two thresholds (assuming for simplicity a deposition rate of K=1) $\bar{c} \pm \Delta c$ for collection and deposition of a detected object. These thresholded rules ensure that robots coordinate their collection of substrate at high values of self-generated photormone field (where robots *have* been recently), while their deposition occurs at low values (where robots *have not* been recently). To allow for nucleation of an aggregation site via a trapping instability, we chose a rotational gain G that permits the formation of traps in the presence of five or more robots. We found this value to facilitate stable yet adaptable nucleation sites that evolve dynamically with the state of the robots and the architectural site.

In Fig. 3(a) we show how the magnitude of the cooperation parameter, $\mathsf{C} \in [0.25, 1]$ (implemented through phototaxis strength), leads to varying architectural patterns while keeping the deposition rate constant at $\mathsf{K} = 1$. It is important to note that the magnitude of C determines the relative significance of phototaxis to exploration such that for small C, the agent performs exploration (see Sec. IV for more details). Initially, RAnts attach to the first substrate element they encounter and carry out a combination of a random walk and gradient ascent as a function of the cooperation parameter [see Fig. 3(a) left panels and SM Video 4]. Once a RAnt with an attached substrate element detects a photormone concentration above the detachment threshold, the element is dropped. We see that higher cooperation, $\mathsf{C} \geqslant 0.5$, leads to higher average curvature, $\bar{\kappa}$ [see Fig. 3(b)], leading to more and more of the RAnts accumulating at the same location. This naturally results in an increase in the rate of aggregation as shown in Fig. 3(c). When C is small, we see a more dispersed deposition pattern [see Fig. 3(a)] leading to a larger average area covered by the formed clusters, $\bar{a}$ [shown in Fig. 3(e)]. When C is large, we see the formation of a single large isotropic cluster, corresponding to the location with a clear peak in the photormone concentration [see Fig. 3(d), SM Sec. VI for details of quantification of the shape of the clusters, also see SM Video 4].

To quantify the robustness of the aggregation algorithm, we vary the strength of phototaxis (captured via C) and the threshold (captured via c^*). In Figs. 4(a) and 4(b), we show the results of these manipulations. With no threshold, i.e., $c^* = 0$, obstacles are randomly dropped in the aggregation area and in particular around the boundary [see Fig. 4(a)]. In the presence of a detachment threshold c^* but without phototaxis $\mathsf{C} = 0$, clusters are formed but the process is very slow. When both the detachment threshold c^* and the phototaxis mechanism is active, $\mathsf{C} = 1$, we observe a coherent final aggregate. The circumference length $L(\lambda_a, \lambda_b)$ [shown in Fig. 4(b)] and the relative area coverage of the largest cluster A_e/A_o [also seen in Fig. 4(b)] capture the robustness of the coupled mechanism when the detachment threshold c^* and phototaxis C are active or inactive. For an inactive threshold corresponding to $c^* = 0$,

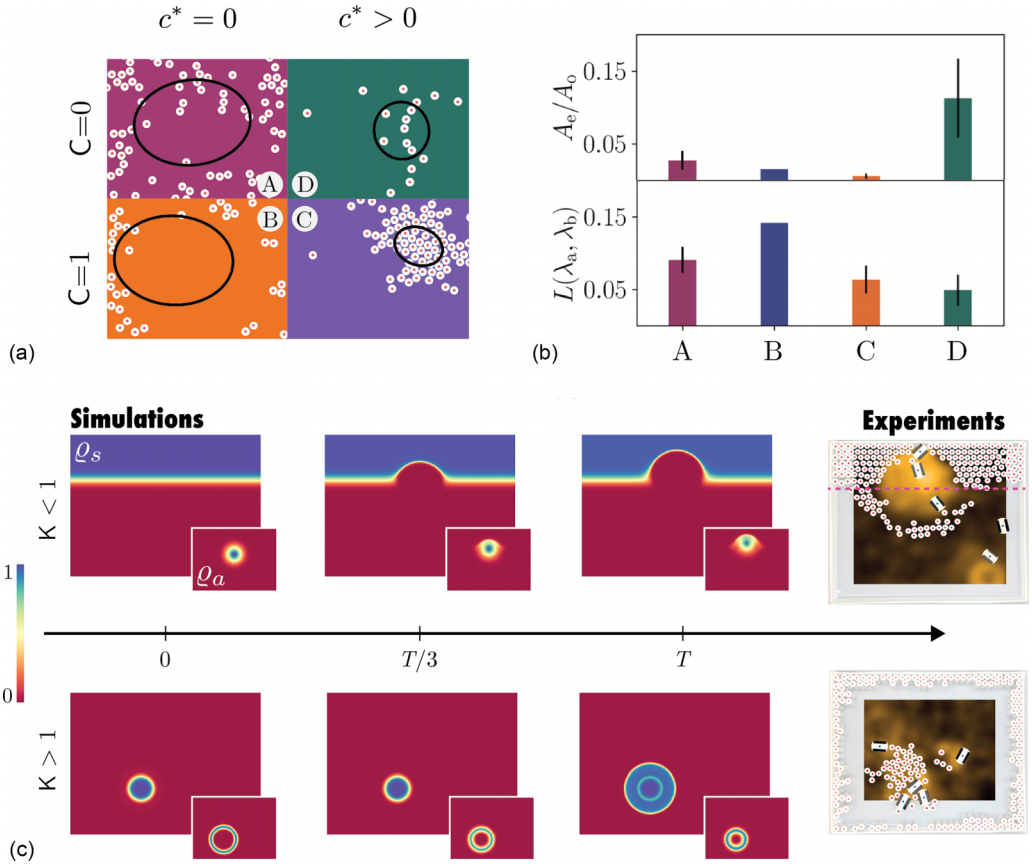


FIG. 4. Robust aggregation with phototactic cooperativity and unified (de)construction phase diagram. (a) Distribution of substrate elements at the end of experiments for four scenarios: (A) with no threshold and phototaxis, $c^* = 0$, $\mathsf{C} = 0$; (B) with no threshold and strong phototaxis, $c^* = 0$, $\mathsf{C} = 1$; (C) with threshold and strong phototaxis, $c^* > 0$, $\mathsf{C} = 1$; (D) with threshold and no phototaxis, $c^* > 0$, $\mathsf{C} = 0$. The black ellipses represent the sample covariance of the substrate elements in the aggregation area. We see that the cluster is densely packed only when both a finite threshold and phototaxis are present, $c^* > 0$ and $\mathsf{C} = 1$. (b) Normalized covered area of deposited substrate, A_e/A_o, for the four cases of collective aggregation studied in (a). (c) Comparison between simulations of Eqs. (8)–(10) showing substrate density ϱ_s (and density ϱ_a in insets) captures both cooperative disaggregation for $\mathsf{K} = -1.44$ and aggregation for $\mathsf{K} = 1.44$ and $\mathsf{C} = 0.8$ (see Sec. IV for simulation details and SM Video 6) and distribution of substrate elements in RAnt experiments under high cooperation, $\mathsf{C} = 1$ for aggregation $\mathsf{K} > 0$ and disaggregation $\mathsf{K} < 0$ (see Appendix 2 for details and SM Video 5). The agent density ϱ_a propagates into the interior of the substrate resulting in degradation of the density ϱ_s for $\mathsf{K} < 0$, while the substrate density ϱ_s grows in magnitude in locations where the agents cluster for $\mathsf{K} > 0$. The tasks exhibited by the RAnt collective are captured in this unified phase space spanned by C and K. Color bar indicates the contour values of ϱ_s.

we generally see elongated ellipses and small clusters (see SM Figs. 3 and 4) that indicate a low cooperative effort and random substrate element deposition. For a case with active threshold $c^* > 0$ but no gradient information $\mathsf{C} = 0$, we do see nearly circular clusters which indicate a localized aggregation effort, with small clusters indicating a cohesive (but slow) aggregation process. Only for an active threshold $c^* > 0$ and gradient information $\mathsf{C} = 1$ do we observe fast, localized, and large aggregates. In addition to c^* and C, the choice and sequence of actions taken by each RAnt during obstacle avoidance can influence both the time required and the robustness of the aggregation. These effects become particularly significant when the density of substrate or RAnts is high in a given region, since the time spent to bypass such bottlenecks determines the local concentration of photormone and its eventual reinforcement, an effect that we do not consider in the current work.

B. Continuum model of collective architectonics

So far we have seen the efficacy and robustness of the chosen interaction rules in the triadic model for collective aggregation in a discrete setting [shown in Fig. 1(a)]. We now capture the dynamics of the collective by averaging over the microscopic behaviors (corresponding to small timescale processes) of the RAnts and arrive at a continuum model to understand the macroscopic behavior of the collective [5]. Our model for collective aggregation involves three interacting spatiotemporal fields, namely the agent density $\varrho_a(\mathbf{x}, t)$, photormone field $c(\mathbf{x}, t)$, and substrate density $\varrho_s(\mathbf{x}, t)$ [shown schematically in Fig. 1(a)]. Our model for the dynamics of cooperative task execution extends the Patlak-Keller-Segel model [5,38] for aggregation in biological systems by accounting for how the architectural environment changes and in-turn modulates RAnt behavior. Here the agent density $\varrho_a(\mathbf{x}, t)$ represents the averaged position of the RAnts

averaged over a characteristic timescale set by the time taken to traverse several domain lengths. The agent density travels with a self-propelled velocity $\mathbf{u}_a$ which is related to the local environment through the relation $\mathbf{u}_a = v_o(1-\varrho_s)\hat{\mathbf{p}}$, where v_o is the speed of the collective and $\hat{\mathbf{p}}$ is its orientation. Just as in the case of RAnts, the velocity of the agents is modified by gradients in photormone concentration due to phototaxis and is given by $\chi\nabla c$, where χ is the phototaxis strength. In the absence of such gradients, since RAnts use an exploratory strategy, their density can diffuse out with diffusivity D_a. We generalize the photormone dynamics in Eq. (5), with k_+, k_- as the rate of production and decay of photormone, by also accounting for its diffusivity, D_c (just as seen in pheromones). The aggregation process is defined as the transportation of substrate elements to locations of high photormone concentration beyond a critical threshold in concentration at a particular location. The dynamics of the substrate density $\varrho_s(\mathbf{x}, t)$ in the aggregation process is captured using a thresholded rate equation where the aggregation rate is given by k_s.

The dynamical equations for $\varrho_a(\mathbf{x}, t)$, $c(\mathbf{x}, t)$, and $\varrho_s(\mathbf{x}, t)$ become (see SM Sec. III for details)

$$\partial_t \varrho_a = -\underbrace{\nabla\cdot(\mathbf{u}_a\varrho_a)}_{\substack{\text{Self-propulsive}\\ \text{advection}}} + \nabla\cdot(\underbrace{D_a\nabla\varrho_a}_{\text{Diffusive flux}} - \underbrace{\chi\varrho_a\nabla c}_{\text{Phototaxis}}), \tag{8}$$

$$\partial_t c = \underbrace{D_c\nabla^2 c}_{\text{Diffusion}} + \underbrace{k_+\varrho_a}_{\text{Production}} - \underbrace{k_- c}_{\text{Decay}}, \tag{9}$$

$$\partial_t \varrho_s = k_s\varrho_s\{\,\Theta\,\underbrace{(c-c^*)}_{\substack{\text{Photormone}\\ \text{field threshold}}}\,\}\times\{\,\Theta\,\underbrace{(\varrho_a-\varrho_a^*)}_{\substack{\text{Robot density}\\ \text{threshold}}}\,\}. \tag{10}$$

In Eq. (10), ϱ_a^* and c^* are the threshold concentration of agent density and photormone field required to initiate aggregation. The threshold behavior that determines the consensus of the agents to start aggregation is captured via the Heaviside function $\Theta(x)$ in Eq. (10). Just as in the case of discrete agents in Eqs. (3) and (4), the cooperation parameter is quantified as the relative strength of phototaxis to diffusion: $\mathsf{C} = \chi c_o/D_a$, with c_o being the reference photormone concentration (discussed in SM Sec. III). The other relevant nondimensional number capturing the task is the nondimensional deposition rate $\mathsf{K} = k_s l/v_o$, where l is the characteristic lengthscale obtained from photormone diffusion-decay dynamics, $l \sim (D_c/k_-)^{1/2}$. We note that in our continuum model, $\mathsf{C} \in [0,\infty)$, $\mathsf{K} \in (-\infty,\infty)$, in contrast to the discrete case where $\mathsf{C} \in [0,1]$, $\mathsf{K} \in [-1,1]$, but both the models capture the same qualitative features. We see in Fig. 4(c) that for $\mathsf{K} > 0$ the collective performs aggregation, whereas for $\mathsf{K} < 0$ it performs disaggregation, i.e., a simple flip in the sign of the deposition rate (associated with agent-environment interaction) results in macroscopically antagonistic tasks. This is indeed what we observe in experiments where the RAnts cooperatively tunnel through a bulk substrate when $\mathsf{K} < 0$ and cooperatively construct when $\mathsf{K} > 0$ [see Fig. 4(c) and also SM Videos 5 & 6]. Together, the cooperation parameter C and the deposition rate K span a two-dimensional phase space of macroscopic behaviors with their boundaries separated by a parametric instability. This allows us to choose from a selection of behaviors that range from coordinated aggregation to scattered construction and collective excavation on the fly by simply tuning these parameters.

V. CONCLUSIONS

We have developed a biologically inspired robotic platform to probe the emergence of collective aggregation and disaggregation behaviors through local interactions and environmental feedback in heterogeneous settings. By designing a system of phototactic robotic agents ("RAnts") coupled to a dynamic light-based communication field ("photormone"), we demonstrated how simple behavioral rules—such as phototaxis and threshold-based transport—can yield functional group-level outcomes such as structure formation, coordinated dismantling, and adaptive spatial patterning.

Identifying and characterizing a trapping instability that drives spontaneous nucleation of aggregation sites allows us to quantify how confinement radius depends on agent gain, sensor geometry, and photormone dynamics. Then we can precisely tune when and how collective behavior emerges as a function of agent density, cooperation strength (C), and deposition rate (K), with relevance for how this might occur in living systems.

We also introduced a unified phase space of behavior for robotic collectives, spanned by C and K, that encodes both cooperative building and excavation within a single framework. This was further extended using a continuum model involving agent density, communication field, and substrate density—generalizing the Patlak-Keller-Segel formalism to aggregation dynamics. Through this multiscale framework, we linked discrete robotic rules to continuum population-level patterns, offering a bridge between experimental robotics and analytical modeling. By adjusting a single microscopic behavioral parameter associated with transporting action at an individual level, robots can switch from building to dismantling structures. Locally tuning the interaction between individuals in these systems introduces flexibility to enable the group to successfully adapt and complete tasks. This approach succeeds even in unpredictable environments that both shape and are shaped by the agents' actions, and it eliminates the need for global planning or optimization. Our results show how small changes in individual actions, when combined with environmental feedback, can drive significant shifts in group behavior. A natural next step is to add functionality that enables outcome selection based on relative fitness—e.g., certain shapes being more effective for specific tasks.

Beyond these specific results, our approach shows that robotics can function as both mirrors and models to understand collective animal behavior. As mirrors, robot collectives may help identify the minimal ingredients required for complex group-level coordination, highlighting the sufficiency of local rules and environmental coupling. As models, they provide a manipulable, reproducible, and measurable platform to test hypotheses about biological systems—ranging under controlled conditions that are often inaccessible in natural settings. By coupling behavioral flexibility at the individual level with emergent adaptability at the group level, our robotic system exemplifies exbodied intelligence, where cognition and coordination arise not solely from agents but from their continual interaction with an evolving environment.

This framework opens up new avenues for engineering autonomous collectives and for systematically interrogating the fundamental principles underlying animal collective intelligence, stigmergy, and adaptive architectural robotectonics.

ACKNOWLEDGMENTS

We thank the NSF PHY1606895 (S.G.P., L.M.), Swiss National Science Foundation P400P2-191115, NSF EFRI 18-30901 (L.M.), NSF 1764269 (L.M.), Kavli Institute for Bionano Science and Technology (L.M.), the Simons Foundation (L.M.) and the Henri Seydoux Fund (L.M.) for partial financial support.

DATA AVAILABILITY

The data that support the findings of this article are openly available [39]; embargo periods may apply.

APPENDIX

1. RAnt design

We designed the robots with the requirement that they are (i) mobile; (ii) capable of sensing substrate elements, other RAnts, and the photormone field; and (iii) capable of transporting substrate elements. We used a rechargeable 3.7 V battery with 400 mAh (Pkcell LIPO 801735) and an Adafruit ItsyBitsy M0 Express microcontroller. Each wheel of the RAnt is 25 mm in diameter and the wheels are driven by brushed dc motors rated at 85 RPM at 3.7 V. A rubber o–ring increases the traction of the wheels. The motor speed is controlled with a Pololu DRV8835 Dual Motor Driver Carrier. Substrate elements are attached to and detached from the robots with a linear servomotor (Spektrum SPMSA2005) that extends and retracts a permanent magnet out of the robot's case. A ferromagnetic ring (3 mm thickness colorFabb SteelFill) embedded in the substrate elements (22 mm × 40 mm PVC cylinders) allows for easy attachment to the permanent magnet when it is extended. RAnts are equipped with two light sensors (Adafruit ALS-PT19) located at the bottom left and right of the RAnt (relative to the direction of travel) and an infrared (IR) distance sensor (Everlight ITR20001 opto interrupter) for obstacle detection up to 3 cm from the sensor. The base of the RAnt is 3D-printed using acrylic styrene acrylonitrile (ASA). The wheel arrangement is inspired by the zooid robots [40] and requires two small steel caster balls 3 mm in diameter to be installed at the base that helps stabilize the RAnt. The 3D-printed case made of ASA protects the RAnt's internal components. A small switch is used to turn the power on/off with the case attached. Blue stickers of 6 mm in diameter placed on top of the RAnts and red stickers on the substrate elements are used for position tracking with the webcam mounted above the arena.

2. RAnt internal rules

The internal rules of the RAnts are summarized in the pseudocode shown in Fig. 2. The program uses a binary variable d that encodes the direction of travel (1 for forward, –1 for backward), the cooperation parameter $\mathsf{C} \in [0, 1]$, the deposition rate $\mathsf{K} \in [-1, 1]$, the high threshold value $c_h = \bar{c} + \Delta c$, the low threshold value $c_l = \bar{c} - \Delta c$, and the maximal detectable photormone value $c_{\max}$.

After the variables are defined, the program enters a while loop that runs until the RAnt is switched off or the battery voltage drops below 3.5 V. The heading of the RAnt is set by adjusting the turning rate as a function of the cooperation parameter and the current sensor readings. Depending on the cooperation parameter, the turning rate is a composition of a random walk and phototaxis and follows the equation

$$\Omega = \frac{\mathsf{C}}{l_s} \tanh\left(\alpha d \mathsf{K} \frac{c_L - c_R}{c_{\max}}\right) + \frac{(1-\mathsf{C})}{l_s} b \sin(\pi W) \quad \text{(A1)}$$

with $l_s = 1$ cm the distance between the left and right sensors, α (=50) a gain parameter, c_L and c_R the photormone intensity measured in the left and right light sensors, respectively, $b = 0.3$ a fixed amplitude, and a stochastic process W (Wiener process). Using a sine function, we map the stochastic process W to the range $[-1, 1]$ to avoid perpetual rotations for large excursions of W. The first term in Eq. (A1) corresponds to phototaxis using the projected photormone, and the second term is a random walk. We can tune the influence of either term with the cooperation parameter C from pure phototaxis at $\mathsf{C} = 1$ to a random walk at $\mathsf{C} = 0$. The deposition rate K defines the success of deposition, and its sign determines whether RAnts construct (positive sign) or deconstruct (negative sign). The turning rate is used to determine the rotational speed of each wheel by

$$\omega_{L,R} = d\left(v_0 \mp G\frac{l_w}{2}\Omega\right), \quad \text{(A2)}$$

with $v_0 = 4$ cm/s the base speed, $G = 10^{-2}$ the rotational gain, and $l_w = 3$ cm the distance between the two wheels. These parameters are chosen in a regime where self-trapping is not possible, but collective trapping is therefore requiring multiple robots to be present to form nucleation sites.

After setting the new heading, the distance sensor is checked for any obstacles that are within 3 cm in front of the RAnt. If an object is detected and the condition $\mathsf{K}\mathsf{C}\, c < \mathsf{K}(\bar{c} - \mathsf{K}\Delta c)$ is satisfied, the RAnt performs a fetching maneuver to attach to the substrate element. After the fetching maneuver, the direction parameter is inverted, i.e., $d = -1$. If an object is picked up with the magnet after the fetching maneuver, the distance sensor will report a detected object as long as it is attached to the magnet. Since $d = -1$, the RAnt will perform the same type of gradient-driven locomotion described in Eqs. (A1) and (A2) but the sign of the signal sent to the motor driver will be inverted, resulting in a reverse motion of the RAnt. If an object is detected, but the photormone concentration does not satisfy the inequality, an avoidance maneuver is performed that consists of a random rotation in place in any direction with the intent to turn away from the detected obstacle.

The next if-statement checks if an obstacle is detected, but without the condition that the direction parameter is equal to 1. If no obstacle is detected, the direction parameter d is set to 1 and the magnet is disengaged. This increases the robustness of the system in case an obstacle is accidentally dropped.

The last if-statement checks whether the RAnt is in the reverse mode $d = -1$ and if the photormone concentration dropped satisfies the inequality $\mathsf{K}\,c > \mathsf{CK}(\bar{c} + \mathsf{K}\Delta c)$. If both statements are true, the magnet is disengaged, depositing any potentially attached wall elements, and the direction parameter is set back to $d = 1$. To avoid the RAnt from reattaching to the just dropped element, it performs a random rotation in place in any direction before returning to the start of the main loop.

3. RAnt experimental setup

The photormone was produced with an Epson EX9200 projector onto an acrylic sheet with a translucent top, which served as the surface on which the RAnts were operating. The projector uses a three-chip digital light processing (DLP), which is required for the light sensors in the RAnts to pick up the photormone field. The dynamics of the photormone field is a function of the RAnt's positions and is given by

$$\partial_t c = k_+ \sum_{i=1}^{n} f(\mathbf{r}_i, w) - k_- c, \tag{A3}$$

with $c = c(\mathbf{x}, t)$ the photormone concentration at position $\mathbf{x} = (x, y)$ and time t, $k_- = 0.02\,\mathrm{s}^{-1}$ the decay rate, $k_+ = 0.1\,\mathrm{s}^{-1}$ the photormone production rate, n the number of RAnts detected in the arena, and $f(\mathbf{r}_i, w)$ a function with the property that it is zero everywhere except around a circle centered around $\mathbf{r}_i$ with diameter $w = 2.5$ cm centered at the geometric center of the ith RAnt. The value of f inside this circle is 1. The positions of the RAnts are used as the centers of sources of photormone. If a RAnt is not moving, photormone is built up with the rate k_+ at that location over time. When the RAnt moves to a new location, the built-up photormone decays with rate k_-. The parameter choice described here has shown to neither saturate the domain with photormone nor be too volatile, but allowing the photormone to act as a spatiotemporal memory for the RAnts over the course of an experiment.

The positions of the RAnts are tracked with a webcam mounted above the arena and evaluated in MATLAB. Blue markers are attached on the centroid of the case's upper surface, which allows us to use a simple blob detection to identify the pixel position of the RAnts. The photormone concentration is then dynamically updated in the same MATLAB script and displayed on the RAnt arena with the projector. The tracking and integration of the photormone field is executed in real time, which restricted the update rate of the projected field to 13 Hz on average. The low refresh rate did not have any noticeable consequences for the conducted experiments.

The setup of the enclosure for the RAnts consisted of solid walls that contained the RAnts within an arena of 67×56 cm^2. A total of 200 substrate elements were distributed along the boundary of the arena and served as the aggregation material. We tracked all substrate elements by attaching a red dot on each of them and tracking them with the webcam. For every experiment, we randomly placed the rants in the arena and waited for the limit of 10 min to be reached. In some cases, we stopped the experiment early due to fast excavation and depletion of the substrate element layer. At that point, data were stored and the experiment ended. There was no leader and no dedicated roles, which made every RAnt replaceable. The aggregation area, that is, the area in which we projected photormone, was 48×35 cm^2. The smaller size ensured that a distinction between the initial substrate element locations and constructed structures can be made. Every element inside the aggregation area will have had to be moved there by a RAnt.

We conducted experiments for five cooperation parameters $\mathsf{C} = \{0, 0.25, 0.5, 0.75, 1\}$ at a fixed excavation rate $\mathsf{K} = 1$ and repeated experiments five times for each parameter. Every RAnt's software was updated before a new set of five experiments with the same cooperation parameter was conducted. The projected photormone field was contained in an area smaller than the full arena to ensure that the RAnts start constructing away from the boundary. For every experiment, we stored the webcam data and time stamps. The video frames were postprocessed, and the locations of all RAnts and wall elements were stored as a function of time.

For the disaggregation experiment, we used $\mathsf{C} = 1$ and $\mathsf{K} = -1$. The only quantities that needed to be modified in the RAnts code were the values of these two parameters. We arranged the substrate elements along the longer edge of the arena, forming seven layers through which the RAnts can excavate before reaching the boundary. Since disaggregation requires an existing substrate element to be excavated at locations of high photormone concentration (which may or may not happen naturally), we initialized the photormone field with a small (∼4 cm diameter) seed at the location of the boundary that decays away at the same rate as regular photormone. This was enough to encourage excavation at the seed's location. We ran the excavation experiment until the first RAnt reached the solid boundary of the arena.

[1] B. Hölldobler and E. O Wilson, *The Ants* (Harvard University Press, Cambridge, MA, 1990).

[2] D. M. Gordon, *Ants at Work: How An Insect Society is Organized* (Simon and Schuster, 1999).

[3] S. Camazine, J.-L. Deneubourg, N. R Franks, J. Sneyd, G. Theraulaz, and E. Bonabeau, *Self-Organization in Biological Systems* (Princeton University Press, Princeton, NJ, 2020).

[4] A. Perna and G. Theraulaz, When social is moulded in clay: On growth and form of social insect nests, J. Exp. Biol. **220**, 83 (2017).

[5] S. G. Prasath, S. Mandal, F. Giardina, J. Kennedy, V. N. Murthy, and L. Mahadevan, Dynamics of cooperative excavation in ant and robot collectives, eLife **11**, e79638 (2022).

[6] R. Pfeifer, M. Lungarella, and F. Iida, Self-organization, embodiment, and biologically inspired robotics, Science **318**, 1088 (2007).

[7] G. Wang, T. V. Phan, S. Li, J. Wang, Y. Peng, G. Chen, J. Qu, D. I. Goldman, S. A. Levin, K. Pienta, *et al.*, Robots as models of evolving systems, Proc. Natl. Acad. Sci. USA **119**, e2120019119 (2022).

[8] A. Miriyev and M. Kovač, Skills for physical artificial intelligence, Nat. Mach. Intell. **2**, 658 (2020).

[9] K. H. Petersen, N. Napp, R. Stuart-Smith, D. Rus, and M. Kovac, A review of collective robotic construction, Sci. Rob. **4**, 28 (2019).

[10] J. P. Desai, J. Ostrowski, and V. Kumar, Controlling formations of multiple mobile robots, in *Proceedings of the 1998 IEEE International Conference on Robotics and Automation* (Cat. No. 98CH36146) (IEEE, Piscataway, NJ, 1998), Vol. 4, pp. 2864–2869.

[11] M. Rubenstein, A. Cornejo, and R. Nagpal, Programmable self-assembly in a thousand-robot swarm, Science **345**, 795 (2014).

[12] S. Li, B. Dutta, S. Cannon, J. J. Daymude, R. Avinery, E. Aydin, A. W. Richa, D. I. Goldman, and D. Randall, Programming active cohesive granular matter with mechanically induced phase changes, Sci. Adv. **7**, eabe8494 (2021).

[13] P.-P. Grassé, La reconstruction du nid et les coordinations interindividuelles chez bellicositermes natalensis et cubitermes sp. la théorie de la stigmergie: Essai d'interprétation du comportement des termites constructeurs, Insectes Soc. **6**, 41 (1959).

[14] A. Heyde, L. Guo, C. Jost, G. Theraulaz, and L. Mahadevan, Self-organized biotectonics of termite nests, Proc. Natl. Acad. Sci. USA **118**, e2006985118 (2021).

[15] M. Dorigo, G. Theraulaz, and V. Trianni, Swarm robotics: Past, present, and future [point of view], Proc. IEEE **109**, 1152 (2021).

[16] M. Gauci, J. Chen, W. Li, T. J. Dodd, and R. Gross, Clustering objects with robots that do not compute, in *Proceedings of the 2014 International Conference on Autonomous Agents and Multi-Agent Systems* (International Foundation for Autonomous Agents and Multiagent Systems, Paris, 2014), pp. 421–428.

[17] C. A. C. Parker, H. Zhang, and C. R. Kube, Blind bulldozing: Multiple robot nest construction, in *Proceedings of the 2003 IEEE/RSJ International Conference on Intelligent Robots and Systems (IROS 2003)* (Cat. No. 03CH37453) (IEEE, Piscataway, NJ, 2003), Vol. 2, pp. 2010–2015.

[18] Y. Song, J.-H. Kim, and D. A Shell, Self-organized clustering of square objects by multiple robots, in *Swarm Intelligence: 8th International Conference*, ANTS 2012, Lecture Notes in Computer Science (LNTCS), Vol. 7461 (Springer, Berlin, Heidelberg, 2012), pp. 308–315.

[19] O. Holland and C. Melhuish, Stigmergy, self-organization, and sorting in collective robotics, Artif. Life **5**, 173 (1999).

[20] F. Iida and F. Giardina, On the timescales of embodied intelligence for autonomous adaptive systems, Annu. Rev. Control Rob. Auton. Syst. **6**, 95 (2023).

[21] I. Rahwan, M. Cebrian, N. Obradovich, J. Bongard, J.-F. Bonnefon, C. Breazeal, J. W. Crandall, N. A. Christakis, I. D. Couzin, M. O. Jackson, *et al.*, Machine behaviour, Nature (London) **568**, 477 (2019).

[22] R. Fujisawa, S. Dobata, D. Kubota, H. Imamura, and F. Matsuno, Dependency by concentration of pheromone trail for multiple robots, in *International Conference on Ant Colony Optimization and Swarm Intelligence*, ANTS 2008, edited by M. Dorigo, M. Birattari, C. Blum, M. Clerc, T. Stützle, and A. F. T. Winfield, Lecture Notes in Computer Science (LNTCS), Vol. 5217 (Springer, Berlin, Heidelberg, 2008), pp. 283–290.

[23] R. Mayet, J. Roberz, T. Schmickl, and K. Crailsheim, Antbots: A feasible visual emulation of pheromone trails for swarm robots, in *International Conference on Swarm Intelligence*, ANTS 2010, edited by M. Dorigo, *et al.*, Lecture Notes in Computer Science (LNTCS), Vol. 6234 (Springer, Berlin, Heidelberg, 2010), pp. 84–94.

[24] A. A. Khaliq, M. D. Rocco, and A. Saffiotti, Stigmergic algorithms for multiple minimalistic robots on an RFID floor, Swarm Intell. **8**, 199 (2014).

[25] A. Reina, M. Salvaro, G. Francesca, L. Garattoni, C. Pinciroli, M. Dorigo, and M. Birattari, Augmented reality for robots: Virtual sensing technology applied to a swarm of e-pucks, in *2015 NASA/ESA Conference on Adaptive Hardware and Systems (AHS)* (IEEE, Piscataway, NJ, 2015), pp. 1–6.

[26] K. Sugawara, T. Kazama, and T. Watanabe, Foraging behavior of interacting robots with virtual pheromone, in *2004 IEEE/RSJ International Conference on Intelligent Robots and Systems (IROS)* (IEEE Cat. No. 04CH37566) (IEEE, Piscataway, NJ, 2004), Vol. 3, pp. 3074–3079.

[27] S. Garnier, F. Tache, M. Combe, A. Grimal, and G. Theraulaz, Alice in pheromone land: An experimental setup for the study of ant-like robots, in *2007 IEEE Swarm Intelligence Symposium* (IEEE, Piscataway, NJ, 2007), pp. 37–44.

[28] F. Arvin, T. Krajník, A. E. Turgut, and S. Yue, Coso: Artificial pheromone system for robotic swarms research, in *2015 IEEE/RSJ International Conference on Intelligent Robots and Systems (IROS)* (IEEE, Piscataway, NJ, 2015), pp. 407–412.

[29] G. Wang, T. V. Phan, S. Li, M. Wombacher, J. Qu, Y. Peng, G. Chen, D. I. Goldman, S. A. Levin, R. H. Austin, *et al.*, Emergent field-driven robot swarm states, Phys. Rev. Lett. **126**, 108002 (2021).

[30] L. Giomi, N. Hawley-Weld, and L. Mahadevan, Swarming, swirling and stasis in sequestered bristle-bots, Proc. R. Soc. A **469**, 20120637 (2013).

[31] J. Aguilar, D. Monaenkova, V. Linevich, W. Savoie, B. Dutta, H.-S. Kuan, M. D. Betterton, M. A. D. Goodisman, and D. I. Goldman, Collective clog control: Optimizing traffic flow in confined biological and robophysical excavation, Science **361**, 672 (2018).

[32] S. Na, M. Raoufi, A. E. Turgut, T. Krajník, and F. Arvin, Extended artificial pheromone system for swarm robotic applications, in *Artificial Life Conference Proceedings* (MIT Press, Cambridge, MA, 2019), pp. 608–615.

[33] See Supplemental Material at http://link.aps.org/supplemental/10.1103/cx3h-bwhc for SI Videos, calculation and simulation details as well as the extended experimental results.

[34] T. C. Schneirla, A unique case of circular milling in ants, considered in relation to trail following and the general problem of orientation, Am Museum Novitates **1253**, 1 (1944).

[35] Y. Tsori and P.-G. De Gennes, Self-trapping of a single bacterium in its own chemoattractant, Europhys. Lett. **66**, 599 (2004).

[36] J. Taktikos, V. Zaburdaev, and H. Stark, Modeling a self-propelled autochemotactic walker, Phys. Rev. E **84**, 041924 (2011).

[37] W. T. Kranz, A. Gelimson, K. Zhao, G. C. L. Wong, and R. Golestanian, Effective dynamics of microorganisms that

interact with their own trail, Phys. Rev. Lett. **117**, 038101 (2016).

[38] T. Hillen and K. J. Painter, A user's guide to PDE models for chemotaxis, J. Math. Biol. **58**, 183 (2009).

[39] https://datadryad.org/stash/share/k3zM3bg_Owr1QvgjX7NjaHJY15GRDbByHH1XAK9e0sE

[40] M. L. Goc, L. H. Kim, A. Parsaei, J.-D. Fekete, P. Dragicevic, and S. Follmer, Zooids: Building blocks for swarm user interfaces, in *Proceedings of the 29th Annual Symposium on User Interface Software and Technology* (Association for Computing Machinery, New York, 2016), pp. 97–109.